Energy &
Environmental
Science

ROYAL SOCIETY
OF CHEMISTRY

www.rsc.org/ees

A hybrid solar-redox scheme for liquid fuel and hydrogen coproduction

Feng He [a], James Trainham[b], Gregory Parsons[a], John S. Newman[b,c], and Fanxing Li*[a]

[a] *Department of Chemical and Biomolecular Engineering, North Carolina State University,*
911 Partners Way, Raleigh, NC 27695-7905, USA.
**Email: Fli5@ncsu.edu*

[b] *RTI International, 3040 E Cornwallis Road, Research Triangle Park, NC 27709-2194*

[c] *Department of Chemical Engineering, University of California, Berkeley, CA 94720-1462*

Abstract

The feasibility of a hybrid solar-redox process, which converts solar energy and methane into separate streams of liquid fuels and hydrogen through the assistance of an oxygen carrier, is investigated via both experiments and simulations. Fixed and fluidized-bed experiments are conducted to evaluate the redox performances of an oxygen carrier composed of iron oxide promoted with a mixed ionic-electronic conductor (MIEC) support. Over 95% conversion in the methane oxidation step and 60% steam to hydrogen conversion in the water-splitting step are observed. Aspen Plus® simulation based on experimental data and a comprehensive set of assumptions estimates the overall process efficiency to be 64.2 – 65.3% on a higher heating value (HHV) basis. Through the integration of solar energy, methane to fuel conversion efficiency can approach 100%. The proposed process has the potential to produce transportation fuels and hydrogen at high efficiency with reduced carbon footprint.

Introduction

Efficient and cost-effective production of clean energy carriers such as hydrogen is of critical importance for sustained growth of the modern economy.[1] Among the various approaches for sustainable hydrogen generation, solar-thermal water-splitting represents a potentially attractive and environmentally friendly option.[2,3] Typical solar-thermal water-splitting schemes involve cyclic redox reactions of transition metal oxides to indirectly convert solar energy and water into separate streams of hydrogen and oxygen. In its simplest configuration, a solar-thermal water-splitting cycle involves two redox steps. In the first step, solar energy is used to decompose a metal oxide at high temperature. In the subsequent step, the decomposed metal/metal oxide is reoxidized with water, producing hydrogen. The key reactions involved in the aforementioned solar-thermal water-splitting cycle include:[4]

$$M_xO_y \rightarrow M_xO_{y-\delta} + \frac{\delta}{2}O_2 \tag{1}$$

$$M_xO_{y-\delta} + \delta H_2O \rightarrow M_xO_y + \delta H_2 \tag{2}$$

Of the two reactions above, Reaction 1 is particularly important from a process design standpoint due to the high temperature required for metal oxide decompositions. From a thermodynamic standpoint, solar-thermal processes have the potential to produce hydrogen at a higher efficiency than the combined power generation – electrolysis approach.[5]

Among the various metal oxide candidates, redox pairs consisting of Fe_3O_4/FeO[6,7] and ZnO/Zn[7–11] have received the most attention. Compared to the Fe_3O_4/FeO redox pair, decomposition of ZnO is more thermodynamically favored. Decomposition temperature of ZnO (~1700 °C) is lower than that of Fe_3O_4.[9] The ZnO/Zn redox pair, however, faces challenges including diffusion limitations in the redox reactions as well as the recombination of Zn vapor and gaseous oxygen during the cooling stage after decomposition (Reaction 1).[12] In addition, material integrity under the extremely high thermal and redox stresses represents another major challenge for the ZnO based redox scheme.[7,13] To date, extensive studies have been performed to address the aforementioned challenges. Although various creative strategies have been proposed and investigated, the economic feasibility of the ZnO based solar-thermal water-splitting cycle is still uncertain.[9,12,14]

Compared to zinc oxides, iron oxides are cheaper and more abundantly available.[6,7,9] In addition, unlike ZnO/Zn, Fe_3O_4 and FeO are nonvolatile and remain in condensed states during the operating cycles.[7] The key challenge of the FeO/Fe_3O_4 water-splitting cycle is the high reaction temperature required for Fe_3O_4 decomposition (2000 °C).[15] The high operating temperature poses significant challenges for reactor design as well as redox material development. Attempts to reduce the decomposition temperature of ferrite materials include the use of mixed oxides with general formula of $M_xFe_{3-x}O_4$[16–19] (M = Mn, Co, Ni, Zn, Mg, etc.). Of particular noteworthiness is the isothermal "hercynite cycle" reported by Muhich et al.[20] which utilizes solid state reactions between ferrite spinel and alumina to tailor the thermodynamic driving forces for the redox scheme. Although these approaches have led to notably lowered decomposition temperatures and/or reduced temperature swings in redox reactions, issues related to metal oxide sintering and deactivations as well as low steam conversion still need to be addressed. To date, the endothermic decomposition reaction for most, if not all, solar-thermal water-splitting processes are conducted at temperatures above 1300 °C.[19] Therefore, novel solar-thermal schemes that can effectively promote metal oxide reduction at lower temperatures are highly desired in order to achieve improved efficiency and economic attractiveness for solar-thermal hydrogen generation.

The reduction or decomposition temperature of metal oxides can be effectively decreased through the introduction of reducing agents such as carbonaceous fuels. The presence of reducing agents significantly lowers the external partial pressure of oxygen (P_{O_2}), thereby enhancing the reduction/decomposition reactions. Among the various potential reducing agents, methane is particularly attractive since it is a clean, relatively cheap, and abundantly available (through natural gas) primary energy source.[21] The use of methane in conjunction with solar energy can notably reduce the carbon footprint of existing methane conversion processes. Moreover, the presence of methane can decrease the reduction temperature of iron oxides to well below 1000 °C.

Steinfeld[22] proposed several high temperature solar-thermal schemes to mitigate CO_2 emission from the metallurgical industry. These process schemes use a combination of methane and solar energy to reduce metal oxides, e.g. iron or zinc oxides, thereby abating the carbon footprint for metal oxide reduction process. It is further proposed that the metal oxides can serve as energy and oxygen carriers (OC) in a cyclic redox process for cogeneration of syngas (from methane oxidation) and hydrogen (from water-splitting).[23] In addition, methanol production using the syngas from solar-assisted methane oxidation has also been discussed.[22,24] Such a combined reduction-reforming approach is particularly attractive since it provides the potential to generate simultaneously hydrogen and methanol with a low carbon footprint. Moreover, the temperature for metal oxide reduction can be significantly lowered when compared to conventional solar-thermal water-splitting processes. Among the several potential metal oxides, iron oxide is considered to be effective, as confirmed by thermodynamic analyses.[23,25,26] To date, experimental studies for iron-oxide-based methane oxidation and water-splitting are relatively limited. Steinfeld et al. studied methane oxidation using iron oxide powders in both a thermo-gravimetric analyzer (TGA) and a fluidized-bed reactor.[23,25] Successful syngas generation from methane was achieved. However, the reactivity of the iron oxide is relatively low, leading to low methane conversions (<35% average conversion).[23,25] In addition, carbon formation occurred when iron oxide is reduced to metallic iron phase. Besides pure iron oxides, a number of iron-containing mixed metal oxides such as ZrO_2-supported Ni-FeO_x[27], Cu−Cr−FeO_x[28], Ni-Cr-FeO_x[29], have been tested. These studies further confirm the reaction chemistry of the combined reduction-reforming scheme. Activities and syngas selectivity of these mixed oxides are nonetheless limited. Unless the reactions are carried out at temperatures significantly above 900 °C, methane conversion is generally below 60% with up to 50% CO selectivity. During the regeneration step, steam conversion is often limited to 25%. Another process of relevance is the so-called chemical looping gasification (CLG) process.[30–32] These processes, however, aim to produce carbon dioxide and hydrogen from methane conversion. Kim et al. comprehensively analyzed a number of novel "Sunshine to Petro" (S2P) process configurations to produce methanol or Fischer-Tropsch (F-T) liquids from solar-thermal CO_2 (and H_2O) splitting.[33,34] Their results indicate that the product costs from optimized S2P processes can be comparable to other renewable-based alternatives. The proposed CO_2/H_2O splitting is performed in absence of methane. Therefore, high operating temperature is likely to be necessary. To summarize, comprehensive experimental and simulation studies of the combined reduction-reforming approach are highly desired.

The current study investigates the feasibility of a hybrid solar-redox process for cogeneration of liquid fuels and hydrogen using methane and solar energy. Similar to the combined reduction-reforming concept[25], the $Fe_3O_4/FeO_{1-\delta}$ redox couple is used for methane (partial) oxidation and water-splitting. In this process, syngas from methane oxidation is used in a Fischer-Tropsch synthesis process for liquid fuel synthesis whereas H_2 from water-splitting is processed as a co-product. The current study reports the redox performances of a novel lanthanum strontium ferrite (LSF) supported iron oxide in a lab-scale tubular reactor. 95% conversion of methane is achieved in the iron oxide reduction step. Steam to hydrogen conversion in excess of 60% is also observed. Results from experimental studies and/or thermodynamic analyses are then used in Aspen Plus simulation models to evaluate the proposed hybrid solar-redox process[35,36].

Proposed redox scheme:

A simplified schematic of the hybrid solar-redox scheme is given in Fig. 1. Solar energy assisted methane conversion is carried out in two interconnected redox steps. In the first step, oxidized ferrite material (Fe_3O_4) is used to convert methane into syngas in a reducer reactor, which reduces Fe_3O_4 to Fe/FeO (or $FeO_{1-\delta}$). The heat required in the reducer is compensated by solar energy. In the subsequent step, reduced ferrite material (Fe/FeO) from the previous step is re-oxidized with steam in an oxidizer, producing concentrated H_2. The syngas produced from Step 1 is then introduced into a Fischer-Tropsch (F-T) reactor to produce a hydrocarbon mixture, which is upgraded in refining units into naphtha and diesel. Hydrogen produced from Step 2 is compressed and purified using a pressure swing adsorption (PSA) system into a final product. A fraction of the hydrogen is used for fuel upgrading in the upgrader. Fuel containing byproducts from the F-T reactor, upgrader, and PSA are combusted for steam generation. A heat recovery steam generator (HRSG) and a series of steam turbines are used to recover process heat and to produce adequate electric power to satisfy parasitic energy requirements. Similar to the combined reduction-reforming approach, the proposed hybrid solar-redox scheme uses methane to supplement solar energy. Besides acting as an energy source, methane provides carbon atoms for liquid fuel synthesis and enables Fe_3O_4 decomposition/reduction at significantly lower temperatures. For instance, decomposition of Fe_3O_4 to FeO is not thermodynamically favored until over 2000 °C. In contrast, methane reduction of ferrites is feasible, both thermodynamically and kinetically, at below 1,000 °C. Besides the lowered operating temperature, the process is able to produce inherently separated liquid fuels and pure H_2. Since a large amount of solar energy is integrated to the methane conversion scheme, the life cycle CO_2 emission from the hybrid solar-redox process is expected to be much smaller than traditional methane-reforming processes.

Integration of solar energy

The experiments carried out in the present study do not involve direct input of solar energy. Instead, an equivalent form of thermal energy is provided by electric heating. It is noted that the proposed process scheme is very similar to the conventional solar-thermal water-splitting processes.[9,22] With significantly lowered operating temperatures and reduced thermal swings, the reactor design can be identical or much simpler for the proposed solar-redox process. A variety of reactor configurations have been investigated for conventional solar thermal water-splitting processes. Among them, the monolithic reactor[37], the foam reactor[38,39], the rotary-type reactor[40] and the volumetric gas–particle solar receiver-reactor[14,41,42] are frequently investigated. The proposed two-step solar-redox process can be carried out in either fixed beds or interconnected fluidized beds as validated in the current study. Therefore, the solar reactor configurations that are particularly suitable for the proposed redox scheme include the rotary-type reactor for fixed bed operation and the volumetric gas-particle solar reactor for fluidized bed operation. Compared to these reactors which have designed operating temperature of over 1400 °C, the reactors in the solar-redox process can be operated at 900 °C or lower. In addition, the MIEC promoted oxygen carrier in the proposed solar-redox process is estimated to be 10 – 20 times more effective (See Table S4 in ESI) than that in conventional solar thermal water-splitting processes.[20,43] As a result, significantly reduced solids inventory and reactor size can be expected. Another potential advantage of the proposed concept is its ability to cope with the intermittency nature of solar energy with ease. Besides the various approaches disclosed in the literature,[35] heat required for methane reforming can be simply compensated by combusting a portion of the reduced iron oxides. Such a strategy allows for continuous process operation in absence of sunlight, at the expense of reduced hydrogen yield. Alternative approaches to ensure continuous operation include: (i) combustion of F-T off-gas and/or supplemental methane; (ii) use of thermal storage material, e.g. alumina sand.[44] As an exploratory study to investigate this novel concept, detailed solar reactor design is outside of the scope.

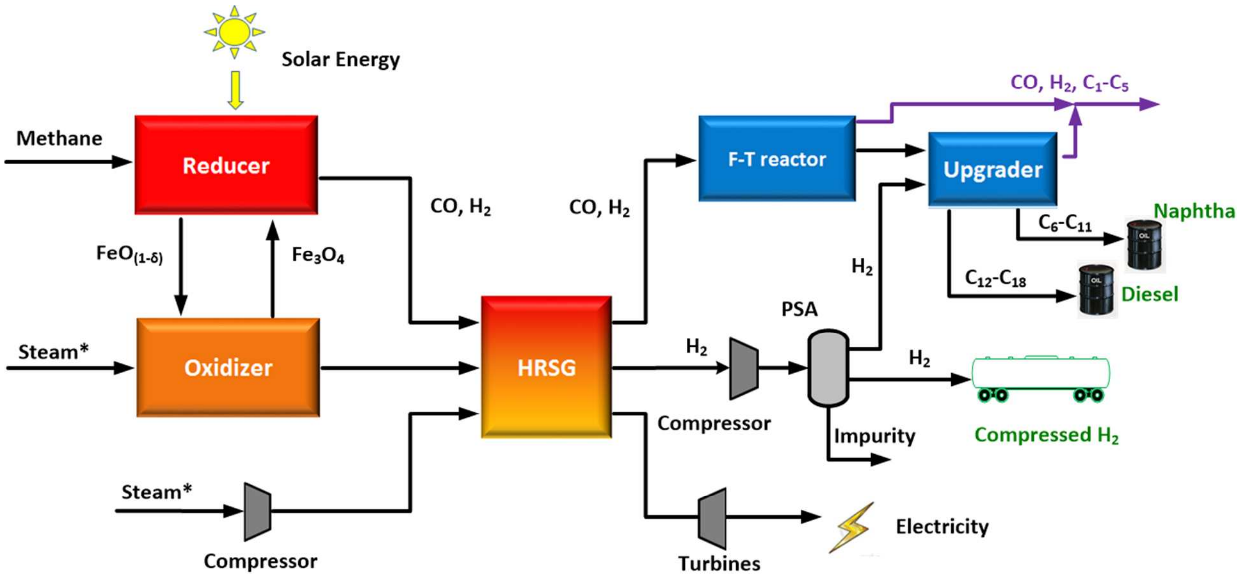

Fig. 1 Simplified schematic of the hybrid solar-redox process. To operate in absence of sunlight, steam* can be (partially) replaced with air to achieve auto-thermal operation.

Experimental and Simulation Methods

Experimental procedure

Lanthanum strontium ferrite ($La_{0.8}Sr_{0.2}FeO_{3-\delta}$ or LSF) supported Fe_3O_4 is used as the redox material, a.k.a. oxygen carrier, for water-splitting. The synthesis method has been reported earlier[45,46] and is described in ESI. Redox experiments are carried out in a tubular reactor (Fig. S1) which can be operated under either fixed-bed or fluidized-bed mode. The quartz reactor tube has an inner diameter of 19 mm and an outer diameter of 25 mm. The reactor is externally heated with a tube furnace (MTI OTF-1200X-S-VT**)**. Temperature inside the reactor is measured using a type K thermocouple. A gas mixing panel with multiple mass flow controllers (MFCs) is used to deliver gaseous mixtures, e.g. nitrogen and methane, to the reactor. Steam is delivered to the reactor through water injection using a syringe pump (KD Scientific model 100) followed by vaporization in the preheating zone of the reactor. Prior to each experiment, 16 mesh silicon carbide (SiC) particles are loaded at the bottom of the reactor to serve as a gas preheater and distributor. The SiC layer also supports the oxygen carrier particles. After loading the SiC particles, 7.5 to 20 grams of iron oxide particles are added on top of the SiC layer. In order to mimic the proposed hybrid redox scheme, the tests are carried out in two consecutive steps, i.e. methane partial oxidation and water-splitting. Both fixed-bed and fluidized-bed operation modes are tested. In typical fixed-bed experiments, the reactor is heated under N_2 flow of 15 ml/min. In fluidized-bed experiments, 600 ml/min of N_2 gas is provided during the heating stage to maintain fluidization of the Fe_3O_4-LSF particles. Once the desired temperature (900 °C unless otherwise specified) is reached, 15 ml/min of methane is introduced to the reactor. Corresponding gas residence times are 2.66 and 0.12 s for fixed-bed and fluidized-bed reactor, respectively. Compositions of the gases exiting the reactor are determined using a gas chromatograph (Agilent Micro GC 490) and a Near-IR gas analyzer (Emerson X-Stream gas analyzer). In order to inhibit excessive carbon formation from methane decomposition, methane injection is stopped when $H_2/(CO+CO_2)$ molar ratio exceeds 2. Water-splitting reaction is carried out after the residue gas from the methane oxidation step has been completely purged with N_2. The water-splitting reaction is initiated by steam injection. 15 ml/min (fixed-bed) or 600 ml/min (fluidized-bed) of N_2 is used as the internal standard. The reaction is stopped when H_2 concentration is below 0.1%. The aforementioned redox reactions are carried out for 5 cycles. The crystal phases of the metal oxides are analyzed using X-ray powder diffraction (XRD) (Rigaku SmartLab) with Cu-Kα (λ=0.1542 nm) radiation in the 20-80° angle range (2θ). The amount of carbon formation is quantified using a Thermal Gravimetric Analyzer (TGA) through combustion of 50 mg sample. The exhaust gas from the TGA is analyzed using a quadruple mass spectrometer (QMS, MKS Cirrus 2). The carbon content is calculated by integrating the CO and CO_2 peaks.

Reactor and process modeling

Aspen Plus[47] is used in the present study to determine the reactor and process performances. Detailed simulation assumptions with respect to materials, simulation modules, property methods, physical property databanks, and key operating parameters are summarized in ESI (Table S1-S3). All the relevant reactions in the proposed reaction scheme are summarized in ESI. Prior to comprehensive process analyses, key reactors, i.e. the reducer and oxidizer are simulated. Sensitive analysis is conducted to investigate the effect of reactor operating conditions using methods reported before.[48,49] F-T reactor is simulated using a RStoic model. The product distribution is determined using the Anderson–Schulz–Flory distribution: $W_n = n(1-\alpha)^2\alpha^{n-1}$. Based on a number of published experimental studies, the α value is assumed to be 0.873 with 80% CO conversion at 10 atm and 220°C.[50–52] After reactor modeling, process simulations are conducted based on specifications provided in Tables S1-S3, where the Aspen Plus flowsheet is shown in Fig. S6. A methane processing capacity of 8 t/hr (tonnes/hour) is assumed for all cases. Such a capacity, which requires solar input of approximately 60 MW_{th}, allows for integration with existing concentrated solar thermal systems,[8,53,38] In order to evaluate the effects of key process parameters, three simulation cases with different operating conditions are simulated. Since the reducer and oxidizer are operated at high temperatures, it is assumed that thermodynamic equilibrium in the two-step reactors can be achieved in two simulation cases (Cases I and II). A kinetically limited case (Case III) is also investigated using the results obtained from experiments. Key operating parameters for the three simulation cases are summarized in Table 1.

Table 1 Operating conditions for the process simulation cases

	Case I*	Case II*	Case III#
Input	8 t/hr CH_4 feedstock and 52-62 MW solar energy usage		
$\dot{n}_{Fe_3O_4} / \dot{n}_{CH_4}$	0.26	0.26	0.64
Reducer temperature and pressure	900 °C, 1 atm	950 °C, 10 atm	900 °C, 1 atm
Oxidizer temperature and pressure	750 °C, 1 atm	750 °C, 10 atm	750 °C, 1 atm

CH_4 conversion	97.6%	95.1%	95 %
Syngas yield	96.5%	93.2%	59%
Steam to H_2 conversion	68 %	68%	60%
Hydrogen purity	100%	100%	97%

* Conversions calculated based on thermodynamic equilibrium

[#] Experimentally obtained conversions (see Table 3). A conservative syngas yield of 59% is used since it is the lowest value observed in fixed bed experiments.

Experimental results

Feasibility of the proposed hybrid solar-redox scheme hinges upon satisfactory performance of the oxygen carrier particles for methane partial oxidation and water-splitting. In order to evaluate the performance of the Fe_3O_4-LSF oxygen carriers, cyclic redox operations are conducted to mimic the proposed reducer and oxidizer operations. Although Fig. 1 illustrates a circulating fluidized-bed type of reactor system where oxygen carriers are circulated between the reducer and oxidizer, the redox scheme can be carried out in fixed-bed reactors in which reactant gases are switched. To investigate the effect of operation modes, both fixed-bed and fluidized-bed operations are investigated in the current study. Five redox cycles are performed under a fluidized-bed mode and five additional cycles are performed under a fixed-bed mode. Post experimental examination indicates that all the particulates are free flowing with no sign of agglomeration. In addition, no oxygen carrier deactivation is identified from the multi-cyclic experiments. Representative experimental data are discussed in the following section. Quantitative parameters for evaluating the redox experiments are summarized in Table 2, where $\dot{n}_i$ represents molar flow rate of component i.

Table 2 Summary of parameters used to characterize the redox reactions

Parameters	Equations
CH_4 Conversion	$(1-\frac{\dot{n}_{CH_4,out}}{\dot{n}_{CH_4,in}})\times 100\%$
H_2/CO ratio	$\frac{\dot{n}_{H_2,out}}{\dot{n}_{\mathrm{CO,out}}}$
Syngas yield	$\frac{\dot{n}_{H_2,out}+\dot{n}_{\mathrm{CO},out}}{3\dot{n}_{\mathrm{CH_4,in}}}\times 100\%$
Steam to H_2 Conversion	$\frac{\dot{n}_{\mathrm{H_2,out}}}{\dot{n}_{\mathrm{H_2O,in}}}\times 100\%$
H_2 Purity	$\frac{\dot{n}_{\mathrm{H_2,out}}}{\dot{n}_{\mathrm{H_2,out}}+\dot{n}_{\mathrm{CO,out}}+\dot{n}_{CO_2,\mathrm{out}}}\times 100\%$

Methane oxidation reaction

Methane conversion and syngas yield for typical fixed-bed and fluidized-bed CH_4 convention experiments are shown in Fig. 3. Further details with respect to the product gas compositions can be found in Fig. S2 (ESI). CH_4 conversion is relatively low at the beginning of the experiments and steadily increase over time. During fixed-bed operations, ~90% methane conversion was observed initially. The instantaneous methane conversion increases to nearly 100% as the reaction proceeds. A similar trend is observed for fluidized-bed operation, which has an initial methane conversion of ~20% and a final conversion of ~60%. The increase in methane conversion is likely to result from the higher activity for methane activation on metallic iron compared to iron oxides. As the reaction proceeds, more reduced iron is available to catalyze methane conversion. Excessive reduction of iron oxides, however, leads to coke formation from methane decomposition reaction. Syngas yield generally correlates with methane conversion at the initial stage of the reaction. Decrease in syngas yield, which corresponds to coke formation, is observed towards the end of the experiment. The average methane conversion under the fixed-bed mode is 95%. The corresponding syngas (CO+H_2) yield is 67% with a H_2/CO molar ratio of ~2. It is noted that both the fluidized-bed and fixed-bed experiments are carried out in a semi-batch mode. Therefore, steady-state gas and solid conversion profiles cannot be established. The very short gas residence time has contributed to the relatively low methane conversion in the fluidized-bed experiments. Improved gas and solids conversions can be expected with larger circulating fluidized-bed reactors. Another observation is the coexistence of notable amount of CO_2 and methane in the gaseous products, especially for the fluidized bed experiment (up to 10% CO_2 and 58% methane, N_2-free basis) as well as the initial stage of the fixed bed experiment (up to 11.5% CO_2 and 3.7% methane, N_2-free basis). This indicates that the Fe_3O_4-LSF oxygen carrier may not be very active for catalytic reforming of methane. Further enhancement of the catalytic activity of the oxygen carrier will likely improve syngas yield, especially for the fluidized bed operations. When compared to previously published experimental data, i.e. about 45% methane conversion and 15% syngas yield,[31] the use of Fe_3O_4-LSF based oxygen carrier has resulted in significantly improved methane conversion and syngas yield.

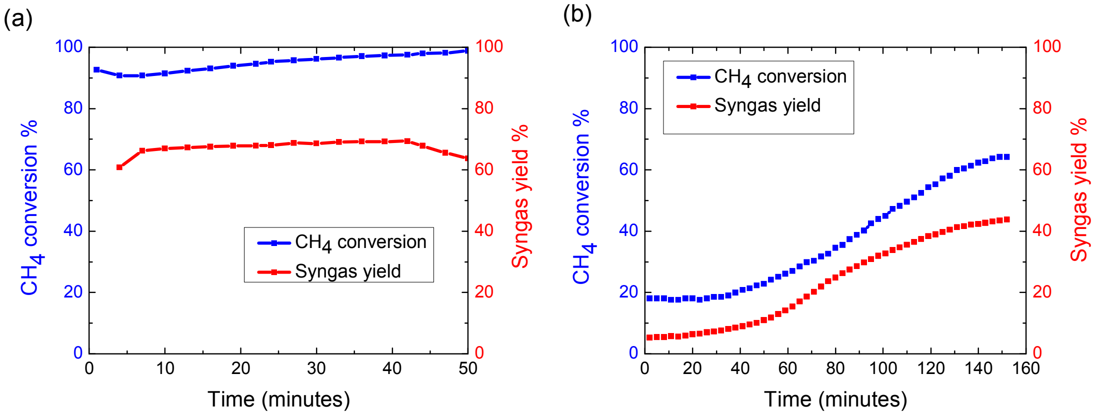

Fig. 2 Methane conversion and syngas yield as a function of time in the CH_4 oxidizing step. (a) 5th cycle fixed-bed (b) 5th cycle fluidized-bed.

Water-splitting reaction

Water-splitting or steam-iron reaction is initiated by introducing steam into the reactor after the methane conversion step. Besides H_2, small amounts of CO and CO_2 are detected, especially within the first 4 minutes of the experiment. This corresponds to the gasification of carbon deposited during the methane conversion step. Fig. 3 shows a representative H_2 purity profile (water-free basis) during the water-splitting step. The overall H_2 purity is 97.2 %. Small amount of the CO and CO_2 are detected at the beginning of the oxidization, which is resulted from coke formed in the methane conversion step. H_2 purity after the first 4 minutes is higher than 99%. A high steam conversion of 55 to 60% is achieved within the first 60 minutes of the oxidation step. Such a conversion is close to the 62.4% steam conversion predicted by thermodynamics. In order to confirm the phase and structural stabilities of the oxygen carrier particles, X-ray powder diffraction (XRD) and carbon analyses are carried out for spent oxygen carriers in both reduced and oxidized forms. XRD spectra of the samples are provided in Fig. S4. Both wustite and metallic iron are observed in the reduced sample whereas the majority of the iron phase in the regenerated sample is magnetite. Iron carbide phases are not identified in the reduced sample, indicating that amorphous carbon and/or carbon fiber may represent the dominant forms of carbon. Post experiment carbon analyses indicate that steam is capable of removing most of, if not all, the carbon formed on the sample during the methane conversion step. Table 3 further summarizes the key experimental data obtained from fixed and fluidized-bed experiments. Experimental data from the 5th redox cycles are shown since the data are quite reproducible among the various redox cycles. The comparisons of the redox performance among different redox cycles are shown in ESI (Fig. S5).

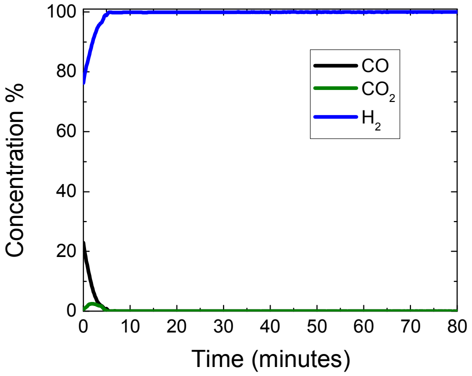

Fig. 3 H_2 concentration (water-free basis) during the water splitting step as a function of time at 900 °C (5th oxidation cycle under fixed-bed mode).

Table 3 Fixed-bed and fluidized-bed results of the redox reactions

	Fixed-bed 5th cycle	Fluidized-bed 5th cycle
Gas residence time (s)	2.66	0.12
Cumulative methane conversion (%)	95.3	38.0
Cumulative syngas yield (%)	67.7	23.0
Syngas production (mmol/gram of OC)	3.1	7.2
Cumulative *H_2/CO* molar ratio	1.9	2.6

Cumulative $(H_2\text{-}CO_2)/(CO+CO_2)$ molar ratio	0.97	1.13
Steam to hydrogen conversion in the first 60 min (%)	60	56.3
Overall steam to hydrogen conversion (%)	47.2	34.2
Cumulative hydrogen purity (%)	97.2	97.5
Carbon Formation (mmol/gram of OC)	0.18	0.24
H_2 yield first 60 min (mmol/gram of OC)	4.3	7.5
H_2 yield (µmol/gram of OC)	5.9	9.6

Aspen Plus® Simulations

The experiments discussed in the previous section confirm the effectiveness of the Fe_3O_4-LSF based oxygen carrier particles for the proposed redox reactions. In the following sections, Aspen Plus simulation is used to estimate reactor and process performances of the hybrid solar-redox concept.

Reactor simulations

Reducer modeling is first conducted at 1 atm and 900 °C using the Aspen Plus RGibbs model. Methane and oxygen carrier particles (Fe_3O_4) are introduced to the reducer. An important parameter characterizing the effectiveness of an oxygen carrier is the molar flow rate ratio between Fe_3O_4 and CH_4, i.e. $\dot{n}_{Fe_3O_4}/\dot{n}_{CH_4}$. Fig. 4 shows H_2/CO ratio, CH_4 conversion, and syngas yield at various $\dot{n}_{Fe_3O_4}/\dot{n}_{CH_4}$. As shown in Fig. 4a, the generation of solid C is inhibited when $\dot{n}_{Fe_3O_4}/\dot{n}_{CH_4}$ is higher than 0.25. In addition, the desired product, i.e. CO and H_2, shows a maximum yield when $\dot{n}_{Fe_3O_4}/\dot{n}_{CH_4}$ is around 0.25 (Fig. 4b), where the H_2/CO molar ratio is about 2. In the process simulations, $\dot{n}_{Fe_3O_4}/\dot{n}_{CH_4}$ equal to 0.26 is selected as the methane to oxygen carrier ratio. Table 4 compares the simulation predicted reducer performance under various temperature and pressure with the experimental data obtained in the fixed-bed. The syngas yield from experiments is significantly lower than that predicted from equilibrium based models. This results from the low catalytic activity of the oxygen carrier for dry reforming of methane. In addition, increase in reducer pressure generally inhibits methane conversion. Steam and/or CO_2 injection can be used to enhance methane conversion and to adjust the H_2/CO ratio to around 2 for Fischer-Tropsch synthesis using a cobalt based catalyst.

The primary function of the oxidizer is to produce hydrogen from steam. The oxidizer model is simulated by a multi-stage RGibbs model reported earlier[48,54]. For the exothermic steam iron reaction, equilibrium steam conversion decreases with increasing temperatures. While pressure has no effect on equilibrium steam conversion, higher molar ratio between reduced iron and wustite ($n_{Fe}/n_{Fe0.947O}$) generally leads to higher steam conversion. At 900 °C and 750 °C, equilibrium steam conversions are estimated to be 62.4% and 68%, respectively.

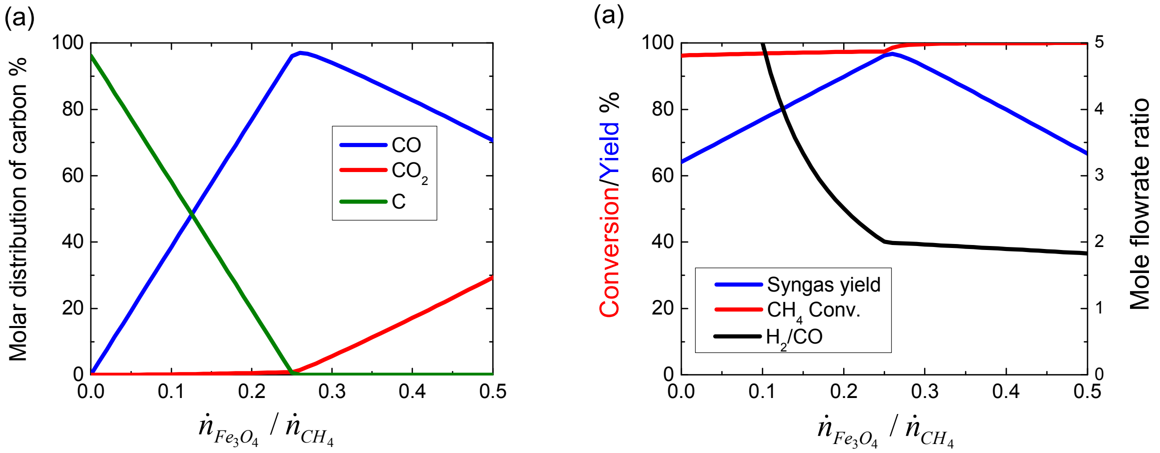

Fig. 4 Reducer performance under various $\dot{n}_{Fe_3O_4} / \dot{n}_{CH_4}$ molar flow rate ratios at 1 atm and 900 °C. (a) Carbon distribution; (b) syngas yield, CH_4 conversion and H_2/CO ratio.

Table 4 Reducer performance under various operating conditions from Aspen Plus simulation and fixed-bed experiments (CH_4 molar flow rate is fixed at 1 kmol/hour).

	Condition A*	Condition B*	Condition C*	Fixed-bed experiment
Temperature	900 °C	900 °C	950 °C	900 °C,
Pressure	1 atm	10 atm	10 atm	1 atm
$\dot{n}_{Fe_3O_4} / \dot{n}_{CH_4}$	0.26	0.26	0.4	N/A
H_2O injection/CH_4	0	0	0.92	0
CO_2 injection/CH_4	0	0	0.27	0
C formation (mmol/g of OC)	0	0	0	0.18
H_2/CO	1.99	1.95	2	1.9
Syngas yield (%)	96.5%	83.0%	88.7%	59 %
CH_4 conversion (%)	97.6%	88.2%	99.3%	95.3%

* Thermodynamic equilibrium is assumed for the reducer under the given temperatures and pressures.

Process Simulations

As specified in Table 1, three simulation cases of the hybrid solar-redox scheme are studied using Aspen Plus. The details of simulation parameters and assumptions are given in the experimental section. Cases I and II assume thermodynamic equilibrium in the redox steps. To evaluate the effect of operating pressure, Case II assumes a higher pressure of 10 atm for the reducer and oxidizer. Case III, a kinetically limited case using experimental data from the fixed-bed reactor, is also investigated using the experimental results presented previously. The process simulation results are summarized in Table 5. Fig. 5 illustrates the energy balances of all three scenarios.

Taking Case I as an example, 8 t/hr CH_4 as well as 52.9 MW concentrated solar energy are converted into 2.0 t/hr naphtha, 3.2 t/hr diesel and 0.984 t/hr compressed hydrogen. As a result, the HHV efficiency of the overall process is 65.1 %. Without considering the solar energy input, the HHV efficiency for methane to fuel/hydrogen conversion is 93.7 %. Such an efficiency is significantly higher than those of conventional gas-to-liquids (GTL) processes, which are typically 57 to 63% efficient on an HHV basis.[55] Case II has hydrogen yields similar to those of Case I. Additional CO_2 and steam are injected into reducer to enhance the CH_4 conversion to 95.3%. Resulting from the reduced requirements for gas compressions, Case II, which operates at 10 atm, has more electricity produced. Therefore, in spite of its inhibition effects for methane conversion, higher operating pressure enhances the overall efficiency of the process. Compared to Cases I and II, Case III produces less liquid fuels and more hydrogen. The overall efficiency of Case III is slightly lower than those of Case I and Case II. Consideration of kinetic limitations has two competing effects: (i) the lower syngas yield of 59% in the reducer leads to decreased liquid fuel production. (ii) Decreased syngas yield in the reducer leads to increased amount of oxygen deficient metal oxides available for water-splitting. This leads to increased hydrogen yield. On a methane conversion basis, the efficiencies of all three cases are significantly higher than those reported for reforming based approaches. Steinfeld et al.[6] evaluated solar-thermal water-splitting process based on Fe_3O_4/FeO redox couples. The maximum efficiency is estimated to be 61% without considering energy losses from product separation, quenching, purification, and F-T synthesis steps. Therefore, the proposed hybrid solar-redox scheme has the potential to utilize methane in a significantly more efficient manner. This corresponds to reduced life cycle greenhouse gas emissions (i.e., carbon footprint) and increased environmental sustainability.

The life-cycle carbon emission of the hybrid solar-redox process and conventional methane reforming processes without CO_2 capture are compared in Table 6. The calculation includes the estimated emission from construction, equipment, fuel transportation and process operation. Emissions from the upstream natural gas production activities are assumed to be 9.1 kg CO_2/mmBtu according to DOE reports.[56,57] As shown in Table 6, the CO_2 footprint of the hybrid solar-redox process (A) is roughly 22 kg CO_2/mmBtu less than hydrogen generation from methane-reforming (B) and 31 kg CO_2/mmBtu less than methane-reforming based liquid fuel generation process (C). When compared with a methane-reforming based hydrogen and liquid fuel co-generation process (D), the CO_2 emission reduction for the hybrid process is 28 kg CO_2/mmBtu less. This translates to 30% less carbon emission than conventional methane reforming for hydrogen and liquid fuel cogeneration. Since the life cycle CO_2 emissions for petroleum-derived gasoline and diesel are around 95 kg CO_2/ mmBtu,[58] a CO_2 emission quota for the liquid fuel products from the solar-redox process can be calculated assuming the synthetic fuels are identical to petroleum derived fuels. When such an emission quota is subtracted, life cycle CO_2 emissions from the H_2 product are estimated to be 4 kg CO_2/mmBtu of H_2 or 95% lower than the conventional scheme. To summarize, the proposed hybrid solar-redox process has the potential to reach high energy conversion efficiency and reduced carbon footprint when compared to traditional approaches based on solar-thermal water-splitting and methane reforming.

Table 5. Process mass and energy balances of the Aspen Plus simulation on the three hybrid solar-redox

	Case I	Case II	Case III
Concentrated solar energy (MW)	52.9	56.9	61.6
CH_4 conversion	97.6%	95.3%	95.3%
Syngas yield	96.5%	93.2%	59%
Syngas (kmol/hr)/(t/hr)	1447/15.5	1399/14.9	878.7/9.66
H_2/CO Ratio	2.0	2.0	1.9
Naphtha (kmol/hr)/(t/hr)	17.4/2.0	15.3/1.8	10.9/1.2
Diesel (kmol/hr)/(t/hr)	15/3.2	13.2/2.8	9.4/2.0
Steam usage (reducer) (t/hr)	0	2.8	0
Steam usage (oxidizer) (t/hr)	13.5	13.5	30.4
Compressed H_2 (kmol/hr)/(t/hr)	487.8/1.0	487.8/1.0	965.6/2.0
Net power (MW)	13.2	3.0	3.5
Overall Efficiency (HHV) %	65.1	65.3	64.2
Efficiency based on methane (HHV) %	93.7	96.1	96.6

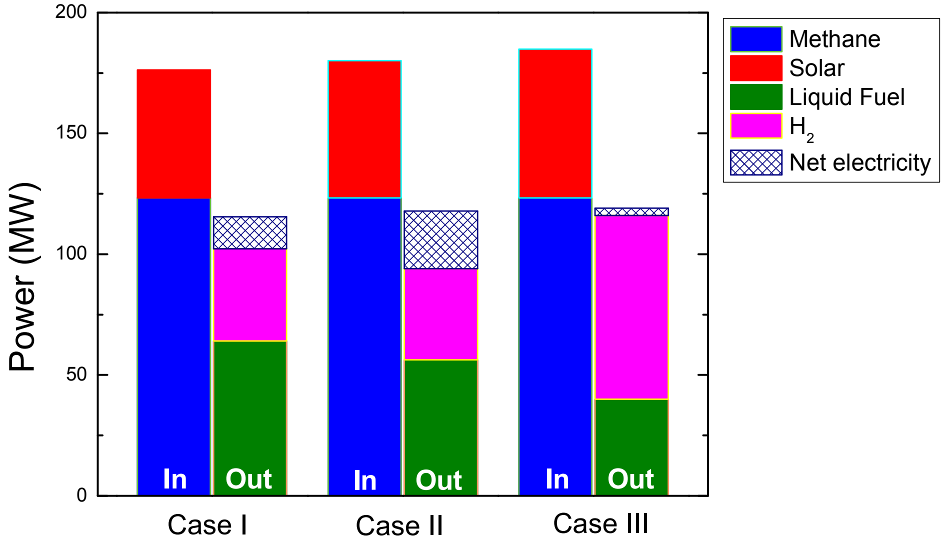

Fig. 5 Energy balances of the hybrid solar-redox processes based on Aspen Plus simulation. (In: energy input into the process; Out: energy output of the process.)

Table 6 Comparison of the process efficiency and life-cycle carbon emission

Process	A	B	C	D
Methane to fuel conversion efficiency	96.6%	70.2%	62.4%	NA
CO_2 footprint kg CO_2/mmBtu	63.9	85.5	95.0	91.7

A: Hybrid solar-redox process (Case III)
B: Methane-reforming for hydrogen generation[56,59]
C: Methane-reforming for liquid fuel generation (GTL)[57]
D: Methane-reforming for hydrogen and liquid fuel cogeneration

Conclusions

The current study investigates a hybrid solar-redox process for liquid fuels and hydrogen cogeneration from methane and solar energy with a mixed ionic-electronic conductor enhanced $Fe_3O_4/FeO_{1-\delta}$ redox couple. Methane is used in the reduction step to enhance iron oxide decomposition/reduction reactions at temperatures significantly lower than those in conventional solar-thermal water-splitting processes. Key findings from the current study are shown below.

The redox performance of a Fe_3O_4-LSF based oxygen carrier is tested in a lab-scale tubular reactor under both fixed and fluidized-bed modes. Repeatable experimental results are obtained over multiple redox cycles for syngas partial oxidation and water-splitting.

At 900 °C, 95% average methane conversion is achieved in the fixed-bed. Syngas with 2:1 H_2 and CO molar ratio, which is ideal for F-T synthesis, can be generated. Hydrogen with overall purity in excess of 97% is generated in the subsequent water-splitting step. The water-splitting step also exhibits high steam to hydrogen conversion. The MIEC enhanced oxygen carrier is 10 – 20 times more effective than those in conventional water-splitting processes, which are carried out at significantly higher temperatures.

Process simulations indicate that high energy conversion efficiencies can be achieved for the solar-redox process under both idealized and kinetically limited scenarios. Under a conservative set of assumptions, the overall process efficiency is estimated to be 64.2 HHV% when considering both methane and solar energy inputs. The methane to fuel efficiency is 96.6 HHV%.

These experimental and simulation studies confirm the feasibility of the proposed hybrid solar-redox scheme. Compared to conventional solar-thermal water-splitting processes, the proposed solar-redox scheme can be carried out at temperatures lower than 1,000 °C with significantly improved kinetics. The reduced operating temperature and simplified energy conversion scheme can result in significantly higher efficiency and lowered carbon footprint when compared to conventional processes.

Acknowledgements

This work is supported by the U.S. National Science Foundation under Award (CBET-1254351), the DOD DURIP Project under Award (61607-CH-RIP), and North Carolina State University

Start-Up Funds. We would like to acknowledge Evan Scott and Kit Yeung in their assistance to set-up the experimental apparatus.

References:

1. H. F. Abbas and W. M. A. Wan Daud, *Int. J. Hydrog. Energy*, 2010, **35**, 1160–1190.
2. T. Nakamura, *Sol. Energy*, 1977, **19**, 467–475.
3. F. Sibieude, M. Ducarroir, A. Tofighi, and J. Ambriz, *Int. J. Hydrog. Energy*, 1982, **7**, 79–88.
4. C. Perkins and A. W. Weimer, *AIChE Journal*, 2009, **55**, 286–293.
5. P. Charvin, S. Abanades, G. Flamant, and F. Lemort, *Energy*, 2007, **32**, 1124–1133.
6. A. Steinfeld, S. Sanders, and R. Palumbo, *Sol. Energy*, 1999, **65**, 43–53.
7. P. Charvin, A. Stephane, L. Florent, and F. Gilles, *Energy Conv. Manag.*, 2008, **49**, 1547–1556.
8. A. Steinfeld, *Int. J. Hydrog. Energy*, 2002, **27**, 611–619.
9. C. Perkins and A. W. Weimer, *Int. J. Hydrog. Energy*, 2004, **29**, 1587–1599.
10. K. Wegner, H. C. Ly, R. J. Weiss, S. E. Pratsinis, and A. Steinfeld, *Int. J. Hydrog. Energy*, 2006, **31**, 55–61.
11. A. Weidenkaff, A. W. Reller, A. Wokaun, and A. Steinfeld, *Thermochim. Acta*, 2000, **359**, 69–75.
12. N. Z. Muradov and T. N. Veziroğlu, *Int. J. Hydrog. Energy*, 2008, **33**, 6804–6839.
13. R. Palumbo, J. Léde, O. Boutin, E. Elorza Ricart, A. Steinfeld, S. Möller, A. Weidenkaff, E. A. Fletcher, and J. Bielicki, *Chem. Eng. Sci.*, 1998, **53**, 2503–2517.
14. J. K. Dahl, A. W. Weimer, A. Lewandowski, C. Bingham, F. Bruetsch, and A. Steinfeld, *Ind. Eng. Chem. Res.*, 2004, **43**, 5489–5495.
15. A. Steinfeld and E. A. Fletcher, *Energy*, 1991, **16**, 1011–1019.
16. Y. Tamaura, A. Steinfeld, P. Kuhn, and K. Ehrensberger, *Energy*, 1995, **20**, 325–330.
17. T. Kodama, N. Gokon, and R. Yamamoto, *Sol. Energy*, 2008, **82**, 73–79.
18. J. R. Scheffe, J. Li, and A. W. Weimer, *Int. J. Hydrog. Energy*, 2010, **35**, 3333–3340.
19. M. Roeb, M. Neises, N. Monnerie, F. Call, H. Simon, C. Sattler, M. Schmücker, and R. Pitz-Paal, *Materials*, 2012, **5**, 2015–2054.
20. C. L. Muhich, B. W. Evanko, K. C. Weston, P. Lichty, X. Liang, J. Martinek, C. B. Musgrave, and A. W. Weimer, *Science*, 2013, **341**, 540–542.
21. P. Setvens, "The 'Shale Gas Revolution': Developments and Changes", 2012. http://www.chathamhouse.org/sites/default/files/public/Research/Energy,%20Environment%20and%20Development/bp0812_stevens.pdf..
22. A. Steinfeld, *Energy*, 1997, **22**, 311–316.
23. A. Steinfeld, A. Frei, and P. Kuhn, *Metall. Mater. Trans. B*, 1995, **26**, 509–515.
24. Y. Katayama and Y. Tamaura, *Energy*, 2005, **30**, 2179–2185.
25. A. Steinfeld, P. Kuhn, and J. Karni, *Energy*, 1993, **18**, 239–249.
26. A. Steinfeld and G. Thompson, *Energy*, 1994, **19**, 1077–1081.
27. T. Kodama, T. Shimizu, T. Satoh, M. Nakata, and K. I. Shimizu, *Sol. Energy*, 2002, **73**, 363–374.
28. S. Takenaka, V. T. Dinh Son, and K. Otsuka, *Energy Fuels*, 2004, **18**, 820–829.
29. S. Takenaka, N. Hanaizumi, V. T. D. Son, and K. Otsuka, *J. Catal.*, 2004, **228**, 405–416.
30. P. Chiesa, G. Lozza, A. Malandrino, M. Romano, and V. Piccolo, *Int. J. Hydrog. Energy*,

2008, **33**, 2233–2245.

31. K. S. Go, S. R. Son, S. D. Kim, K. S. Kang, and C. S. Park, *Int. J. Hydrog. Energy*, 2009, **34**, 1301–1309.
32. L.-S. Fan and F. Li, *Ind. Eng. Chem. Res.*, 2010, **49**, 10200–10211.
33. J. Kim, C. A. Henao, T. A. Johnson, D. E. Dedrick, J. E. Miller, E. B. Stechel, and C. T. Maravelias, *Energy Environ. Sci.*, 2011, **4**, 3122–3132.
34. J. Kim, T. A. Johnson, J. E. Miller, E. B. Stechel, and C. T. Maravelias, *Energy Environ. Sci.*, 2012, **5**, 8417–8429.
35. F. Li and L.-S. Fan, *Energy & Environ. Sci.*, 2008, **1**, 248.
36. L.-S. Fan, *Chemical Looping Systems for Fossil Energy Conversions*, John Wiley & Sons, 2010.
37. M. Roeb, A. G. Konstandopoulos, A. Steele, P. Stobbe, C. Agrafiotis, C. Sattler, R. Klüser, V. T. Zaspalis, L. Nalbandian, N. Monnerie, and L. de Oliveira, *J. Sol. Energy Eng.*, 2005, **128**, 125–133.
38. T. Kodama, *Prog. Energy Combust.*, 2003, **29**, 567–597.
39. T. Kodama and N. Gokon, *Chem. Rev.*, 2007, **107**, 4048–4077.
40. R. B. Diver, J. E. Miller, M. D. Allendorf, N. P. Siegel, and R. E. Hogan, *J. Sol. Energy Eng.*, 2008, **130**, 041001–041001.
41. N. Gokon, S. Takahashi, H. Yamamoto, and T. Kodama, *Int. J. Hydrog. Energy*, 2008, **33**, 2189–2199.
42. A. Steinfeld, M. Brack, A. Meier, A. Weidenkaff, and D. Wuillemin, *Energy*, 1998, **23**, 803–814.
43. T. Kodama, Y. Nakamuro, and T. Mizuno, *J. Sol. Energy Eng.*, 2004, **128**, 3–7.
44. Support for Cost Analyses on Solar-Driven High Temperature Thermochemical Water-Splitting Cycles. 2011 TIAX LLC. https://www1.eere.energy.gov/hydrogenandfuelcells/pdfs/solar_thermo_h2_cost.pdf
45. N. L. Galinsky, Y. Huang, A. Shafiefarhood, and F. Li, *ACS Sustainable Chem. Eng.*, 2013, **1**, 364–373.
46. A. Shafiefarhood, N. Galinsky, Y. Huang, Y. Chen, and F. Li, *ChemCatChem,* 2014, **6**, 790-799.
47. Aspen Technology Inc. ASPEN Plus v7.2 user guide. Aspen Technology, Inc. Cambridge, MA. 2006.
48. L. Zeng, F. He, F. Li, and L.-S. Fan, *Energy Fuels*, 2012, **26**, 3680–3690.
49. F. He, N. Galinsky, and F. Li, *Int. J. Hydrog. Energy*, 2013, **38**, 7839–7854.
50. P. J. vanBerge and R. C. Everson, *Natural Gas Conversion IV*, 1997.
51. S. T. Sie, *Rev. Chem. Eng.*, 1998, **14**, 109–157.
52. D. Gray, J. Klara, G. Tomlinson, and C. White, "Chemical-Looping Process in a Coal-to-Liquids Configuration", DOE/NETL-2008/1307. http://www.netl.doe.gov/energy-analyses/pubs/DOE%20Report%20on%20OSU%20Looping%20final.pdf.
53. S. Möller, D. Kaucic, and C. Sattler, *J. Sol. Energy Eng.*, 2005, **128**, 16–23.
54. F. Li, L. Zeng, and L.-S. Fan, *Fuel*, 2010, **89**, 3773–3784.
55. L. Bibber, J. Haslbeck, S. Kramer, and S. Olsen, "Technical and Economic Assessment of Small-Scale Fischer-Tropsch Liquids Facilities", DOE/NETL-2007/1253. http://www.netl.doe.gov/energy-analyses/pubs/Small-Scale%20F-T%20Liquids%20Facilities_Final.pdf.
56. J. Ruether, M. Ramezan, and E. Grol, "Life-Cycle Analysis of Greenhouse Gas Emissions for

Hydrogen Fuel Production in the United States from LNG and Coal", DOE/NETL-2006/1227. http://www.netl.doe.gov/energy-analyses/pubs/H2_from_Coal_LNG_Final.pdf.

57. E. Shuster and J. Goellner, "Analysis of Natural Gas-to-Liquid Transportation Fuels via Fischer-Tropsch", DOE/NETL-2013/1597. http://www.netl.doe.gov/energy-analyses/pubs/Gas-to-Liquids_Report.pdf.
58. K. Gerdes, T. Skone, NETL's Capability to Compare Transportation Fuels: GHG Emissions and Energy Security Impacts, DOE/NETL, 2009. http://www.netl.doe.gov/energy-analyses/pubs/Petroleum%20Fuels%20GHG%20Modeling_Feb%2025a.pdf.
59. W. Feng, P. Ji, and T. Tan, *AIChE Journal*, 2007, **53**, 249–261.

Investigation of a hybrid solar-redox scheme for liquid fuel and hydrogen coproduction

Feng He [a], James Trainham[b], Gregory Parsons[a], John S. Newman[b,c], and Fanxing Li*[a]

[a] *Department of Chemical and Biomolecular Engineering, North Carolina State University,*
*911 Partners Way, Raleigh, NC 27695-7905, USA. *Email: Fli5@ncsu.edu*
[b] *RTI International, 3040 E Cornwallis Road, Research Triangle Park, NC 27709-2194*
[c] *Department of Chemical Engineering, University of California, Berkeley, CA 94720-1462*

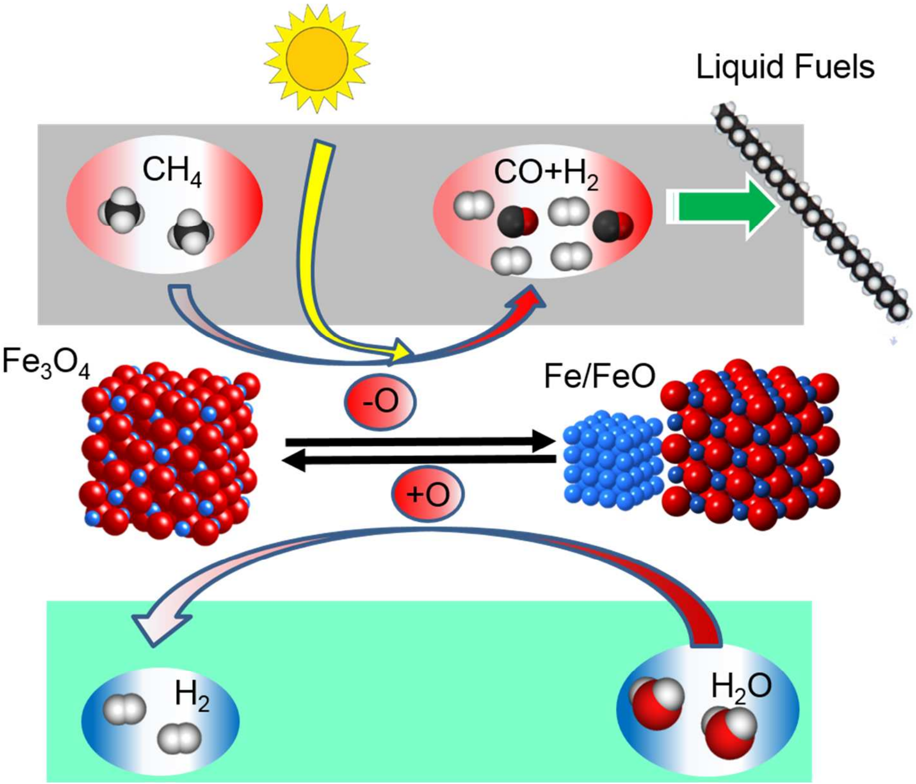

Graphical Abstract

A ferrite based oxygen carrier promoted with a mixed ionic-electronic conductor support is used in a hybrid solar-redox scheme for liquid fuel and hydrogen co-production from methane and solar energy. Compared to typical oxygen carriers for solar-thermal water-splitting, the oxygen carrier reported is 10 – 20 times more effective. Based on both experiments and simulations, the hybrid scheme has the potential to co-produce liquid fuels and hydrogen at high efficiency with near zero life cycle CO_2 emission for the hydrogen product.